3-30-2005

Observations of Gravity Wave Breakdown into Ripples Associated with Dynamical Instabilities

Feng Li
University of Illinois at Urbana-Champaign

Alan Z. Liu
Embry Riddle Aeronautical University - Daytona Beach, liuz2@erau.edu

Gary R. Swenson
University of Illinois at Urbana-Champaign

James H. Hecht
The Aerospace Corporation

Walter A. Robinson
University of Illinois at Urbana-Champaign

Observations of gravity wave breakdown into ripples associated with dynamical instabilities

Feng Li,[1] Alan Z. Liu,[2] Gary R. Swenson,[2] James H. Hecht,[3] and Walter A. Robinson[1]

Received 1 April 2004; revised 18 November 2004; accepted 4 February 2005; published 30 March 2005.

[1] The breakdown of a high-frequency quasi-monochromatic gravity wave into small-scale ripples in OH airglow was observed on the night of 28 October 2003 at Maui, Hawaii (20.7°N, 156.3°W). The ripples lasted ~20 min. The phase fronts of the ripples were parallel to the phase fronts of the breaking wave. The mechanism for the ripple generation is investigated using simultaneous wind and temperature measurements made by a sodium (Na) lidar. The observations suggest that the wave breaking and the subsequent appearance of ripples were related to dynamical (or Kelvin-Helmholtz) instabilities. The characteristics of the ripples, including the alignment of the phase fronts with respect to the wind shear, the motion of the ripples, and the horizontal separation of the ripple fronts were consistent with their attribution to Kelvin-Helmholtz billows. It is likely that the dynamical instability was initiated by the superposition of the background wind shear and the shear induced by the wave. The wind shear, the mean wind acceleration, and the propagation of the breaking wave were found to be in the same direction, suggesting that wave-mean flow interactions contributed significantly to the generation of the strong (>40 m/s/km) wind shear and instability.

Citation: Li, F., A. Z. Liu, G. R. Swenson, J. H. Hecht, and W. A. Robinson (2005), Observations of gravity wave breakdown into ripples associated with dynamical instabilities, *J. Geophys. Res.*, *110*, D09S11, doi:10.1029/2004JD004849.

1. Introduction

[2] Short-period, quasi-monochromatic disturbances are ubiquitous in mesopause airglow layers, as reported by numerous airglow imager observations [e.g., *Peterson*, 1979; *Taylor and Hill.*, 1991; *Swenson and Espy*, 1995; *Walterscheid et al.*, 1998]. Most short-period disturbances fall into two categories, bands and ripples [*Taylor et al.*, 1995]. The band structures often appear as a train of wave fronts with a horizontal wavelength of tens of kilometers. The ripples are small-scale structures with a horizontal separation of less than ~15 km. It is believed that the band structures are atmospheric gravity waves (AGWs) originating from the lower atmosphere, and the ripples are generated in situ by convective or dynamical instabilities (see, e.g., *Taylor and Hapgood* [1990], *Nakamura et al.* [1999], and the review by *Hecht* [2004]). Because instabilities are important in wave breaking, studying how ripples are generated will lead to improved understanding of the dynamics of the upper mesosphere and lower thermosphere (MLT) region.

[3] Depending on how they are generated, ripples display different alignments of their phase fronts with respect to their accompanying wave band and to the background wind shear. Ripples have been observed which were aligned perpendicular to short-period, short-wavelength bands in OH airglow [*Hecht et al.*, 1997, 2000]. These ripple events were associated with the breakdown of long-period, long-wavelength AGWs identified in simultaneous lidar observations. By comparing the observations with model simulations, it was argued that the ripples were generated by convective instabilities [*Fritts et al.*, 1997; *Hecht et al.*, 1997]. Very different ripple structures were observed by *Hecht et al.* [2001], who found that the ripples were aligned parallel to the short-period wave bands. They suggested that these ripples were Kelvin-Helmholtz (KH) billows produced by a shear instability that developed as the result of an AGW approaching a critical level. These studies indicate the importance of simultaneous temperature and wind measurements in investigating the generation of the ripples. In addition, such observations provide an opportunity for assessing the effects of breaking waves on the mean flow during a ripple event [e.g., *Fritts et al.*, 2002].

[4] High-resolution temperature and wind measurements are essential for ripple studies. Recent observations reveal that strong wind shears capable of causing dynamical instability often exist in a narrow layer with a depth of ~2 km [*Li et al.*, 2005]. The Maui/Malt atmospheric observatory was established recently on Mt. Haleakala on Maui, HI (20.7°N, 156.3°W). The instrumentation in the observatory includes airglow imagers, a meteor radar and a Na wind/temperature lidar. Simultaneous and independent lidar and airglow measurements provide unique data sets with the high resolution necessary for investigating instabilities in the mesopause region.

[1]Department of Atmospheric Sciences, University of Illinois at Urbana-Champaign, Urbana, Illinois, USA.
[2]Department of Electrical and Computer Engineering, University of Illinois at Urbana-Champaign, Urbana, Illinois, USA.
[3]Space Science Application Laboratory, The Aerospace Corporation, Los Angeles, California, USA.

0148-0227/05/2004JD004849$09.00

[5] Using data from a Maui/MALT campaign in July 2002, *Hecht et al.* [2005] reported high temporal-resolution observations of ripple structures that developed from a dynamical (wind shear–induced) instability. These ripples, which passed directly over the lidar beam, were shown to be the manifestation of KH billows. These observations allowed, for the first time, a study of the evolution and breakdown of KH billows at mesopause altitudes. The formation of the dynamical instability, however, was not associated with any specific AGW.

[6] In this paper, using Maui/MALT data from 28 October 2003, we report observations of a gravity wave breakdown into ripples in the OH airglow. This is the first time direct observations of gravity wave breaking and subsequent instability generation in the airglow. Unlike the case of *Hecht et al.* [2001] which produced ripples due to an AGW approaching a critical level, these observations definitively show that the breakdown of the AGW itself, well away from any critical level, caused a dynamical instability to form, resulting in the production of ripples. The origin of the large wind shear in the dynamically unstable layer and the acceleration of the mean flow due to the breaking wave are also explored.

2. Instrumentation

2.1. OH Airglow Imager

[7] An all-sky airglow imager was installed on Mt. Haleakala in January 2002 and has been taking data during low moon periods since then. This imager is similar to the airglow imaging system described by *Rezaul and Swenson* [1999]. It incorporates an all-sky lens with an Apogee 1024 × 1024 CCD camera to take images of the all sky field. A broadband filter (750.0–930.0 nm with a notch at 865.0 nm) is used to measure the mesospheric hydroxyl (OH) airglow emission which is centered at a mean altitude of ~87 km. The exposure time is 60 sec and images are taken every 2 min. The images are binned to 512 × 512 pixels to increase the signal-to-noise ratio.

[8] Another airglow imager, developed by the Aerospace Corporation, was also located on Mt. Haleakala. This camera is described in the work of *Hecht et al.* [2005]. This camera combines a custom wide-angle lens with a 256 × 256 HgCdTe detector array, cryogenically cooled, to provide images over an approximately 73 × 73 degree region of the sky. 128 pixels across the center is approximately equal to 40 degrees or 61 km at 85 km altitude. The detector, NICMOS3 device developed by Rockwell Science Center, is identical to the devices by the same name that are currently operating on the Hubble Space Telescope. The array consists of four 128 × 128 quadrants each with its own readout circuitry. Unfortunately, one 128 × 128 pixel quadrant has been lost. Within the cryogenic camera cell is a broadband astronomical "H" filter (1550–1750 nm) that transmits the output of the external filter. This "H" filter is sandwiched with a custom blocking filter that moves the red edge to 1700 nm and considerably reduces the thermal background. For this experiment a fixed open filter position was used allowing the OH Meinel band emission in this wavelength range to be imaged. Images were exposed for about 1.5 s and images were obtained approximately every 3 s. One-minute time difference images were created for comparison with the Illinois camera described above.

2.2. Na Wind/Temperature Lidar

[9] The University of Illinois Sodium (Na) wind/temperature lidar system [*Gardner and Papen*, 1995] is colocated with the all-sky airglow imager on Mt. Haleakala. Coupled with a steerable 3.67 m diameter astronomical telescope at the Air Force Maui Optical Station, the lidar system measures the line-of-sight (LOS) Na density, Doppler temperature, and Doppler wind profiles in the 80–105 km height range. The lidar is pointed to the zenith (Z), and 30° off the zenith toward north (N), east (E), south (S) and west (W) in ZNEZSW sequence. Horizontal winds are derived from off-zenith LOS wind profiles, while the zenith LOS wind gives the vertical wind. The temporal resolution of measurements is ~2 min.

[10] On the night of 28 October 2003, the lidar made measurements between 0530 and 1545 UT. For this study, all profiles were smoothed using a 1 km Hamming window with a 0.5 km resolution in the vertical. The vertically smoothed profiles were then binned temporally to form a smoothed set of profiles with a 15 min resolution. Except where noted, this is the basic data set we use in this study. Average uncertainties are 0.4 K and 1 m/s at the center of the Na layer (~92.5 km), and they increase to 1 K and 3 m/s at the edge of the Na layer (~85 and 100 km) for temperature and horizontal winds. Measurement uncertainties increase sharply below 85 km and above 100 km. Only the observations between 85 and 100 km are discussed in this paper.

3. Results

3.1. OH Airglow Observations

3.1.1. Overview of the Night

[11] Figure 1 shows keograms of time difference airglow images observed on 28 October 2003, which summarize gravity wave activity for the night. The north-south keogram shows coherent wave structures after ~1000 UT. Wave fronts first appeared on the northern horizon and moved southward and disappeared off the southern horizon. Wave bands can also be seen in the east-west keogram when waves propagated from west to east, but exhibited little phase change between 45° off the zenith, indicating that the waves were propagating mainly southward. These wave structures consisted of several wave trains. The wave bands that crossed the zenith between ~1100 and 1300 UT had a shorter period than those between ~1340 and 1440 UT. The latter wave is of particular interest, because its leading front was much brighter than the following wave fronts. Another bright wave front passed the zenith at ~1500 UT, indicating the start of a new wave train. The east-west keogram also shows the existence of very fine-scale ripple structures between ~0900 and 1000 UT covering the whole sky and between ~1440 and 1500 UT in the east portion of the sky. We focus on the latter ripple event in this paper, since the sky was partly cloudy during the first event.

3.1.2. Observations of Ripples

[12] A sequence of all-sky OH airglow images between 1428 and 1450 UT are shown in Figure 2. These images reveal complex wave activities with multiple wave trains

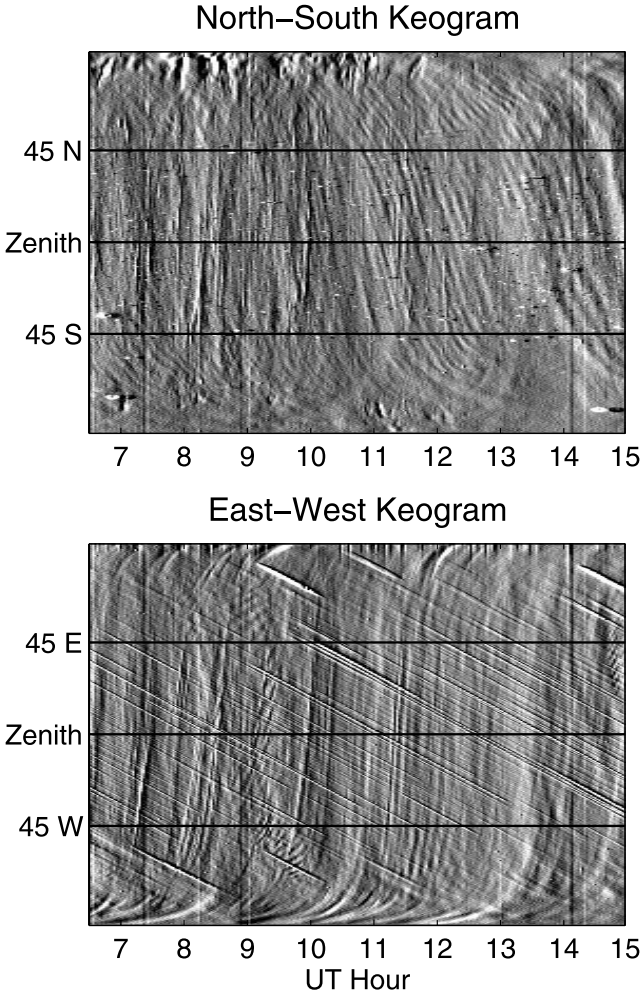

Figure 1. Keograms on the night of 28 October 2003. A keogram is constructed from time difference all-sky OH airglow images, where a time difference image is the difference between two subsequent raw images. The mean of the central 10 columns (rows) of each time difference image is concatenated as a function of time to form the north-south (east-west) keogram. Locations of the zenith, 45° north (east) and 45° south (west) off zenith, are indicated on the north-south (east-west) keogram. Assuming that the OH airglow layer is centered at ~87 km, the distance between 45° north (east) and 45° south (west) is ~174 km. Keograms summarize gravity wave activity for a night. The sinusoid structures are gravity wave fronts. Note that the straight lines moving westward with time on the east-west keogram are star tracks.

crossing the sky before and during the ripple event. The wave structures are more readily recognized by watching the movie sequence of the images. In order to help in identifying the wave trains, propagation directions and major phase fronts of four waves are sketched in the first image at 1428 UT. Wave A propagated toward the SE. Four bright fronts of wave A were seen in the NW quadrant. The leading front of wave A almost overtook the trailing front of wave D, which was moving SSE. Wave C occupied the southern sky and propagated SSW. Three phase fronts of wave B were clearly seen in the SE quadrant. The northern parts of wave B overlapped with wave D, while the southern portions of wave B overlapped with wave C. This complicated wave structure changed dramatically after 1434 UT.

[13] The first signature of ripples appeared at 1434 UT, when the southern part of the east most front of wave B began to break into small-scale structures. In the subsequent images, other phase fronts of wave B broke. The breakdown of the middle front into ripples is clearly seen at 1438 UT. By 1442 UT ripples completely replaced wave B. The phase fronts of the ripples were aligned nearly parallel to the phase fronts of wave B. The ripples occupied a patch of sky with a size ~100 × 150 km. The ripple patch drifted NE until 1458 UT, when the imager was shut down (images after 1450 UT are not shown). The breaking of wave B and the evolution of the ripples had a large impact on the structures of wave A, C and D. Wave D was hardly recognizable after 1440 UT. Phase fronts of wave A and C were distorted.

[14] Figure 3 shows the time evolution of airglow brightness features perpendicular to the phase fronts of wave B. Three wave fronts of wave B and their phase propagation from right to left are clearly seen before 1434 UT. The disappearance of wave B and the transition into fine-scale ripples occurred at 1436 and 1438 UT. After 1440 UT, wave B was replaced by ripples. Figure 3 shows clearly that the breaking of wave B produced the ripples. Also supporting this is the orientation of the wave fronts. Note that the east most front of wave B was oriented at a small angle to the other two fronts (see images before 1434 UT). The alignments of the ripple fronts show a similar feature, in that the orientation of the ripples in the eastern portion of the image has a slightly larger east-west component than those near the center.

[15] Although ripples are not uncommon in airglow measurements, observations of the breakdown of AGWs into ripples are rare. *Yamada et al.* [2001] reported an AGW breaking into turbulence in OH airglow. During the transition from a quasi-monochromatic AGW to chaotic structures, small-scale instability structures were observed aligned with the fronts of the breaking wave. These small-scale instability structures are different, however, from typical ripples in that they quickly broke into random turbulence. Our observations show clearly that the ripples resulted from wave breaking. The horizontal wavelength (λ_h), observed phase speed, and the observed period of the breaking wave were ~44 km, ~50 m/s, and ~15 min, respectively. Assuming the background wind in the OH airglow layer is the average of the wind between 85 and 90 km, the intrinsic phase speed and intrinsic period of wave B were ~90 m/s and ~8 min, respectively. The vertical wavelength (λ_z), calculated using linear gravity wave dispersion relation, was ~35 km, indicating wave B was upward propagating. These values are typical for AGWs observed by airglow imagers [e.g., *Swenson et al.*, 2000].

[16] This ripple event was also observed by the Aerospace airglow camera. Figure 4 shows a sequence of time difference images between ~1440 and 1450 UT. Because of a smaller field-of-view and the loss of data in a quadrant, the Aerospace camera did not observe the breakdown of the parent wave into ripples, but it clearly recorded the ripples and their movement when the ripples approached the zenith after ~1440 UT. The first image at 143937 UT shows three ripple fronts in the right of the image which were oriented

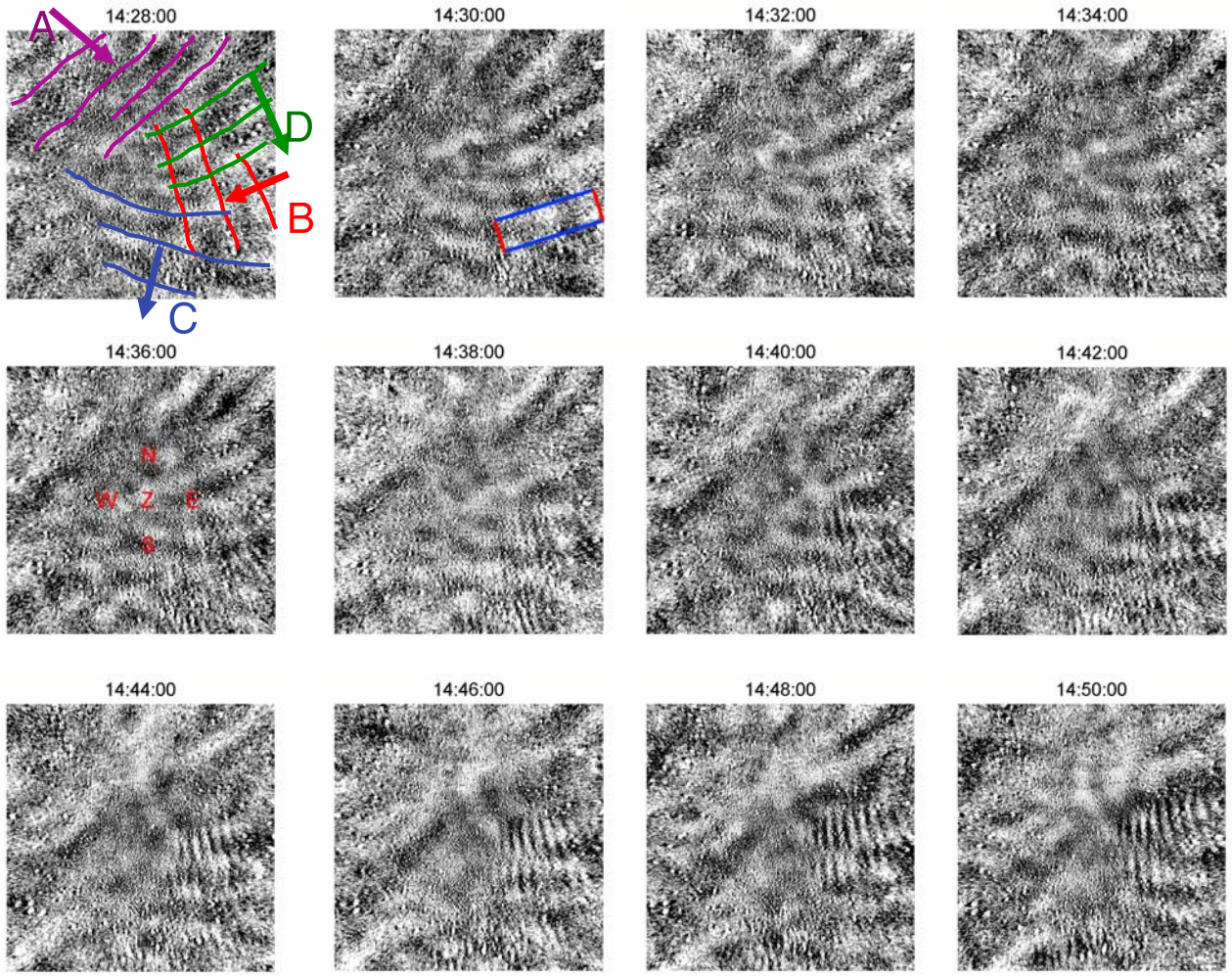

Figure 2. A sequence of unwarped all-sky OH airglow images between 1428 and 1450 UT. The observation UT time is given at the top of each image. North is at the top and east is to the right of each image. The center of the image corresponds to the zenith. Each image has been flat-fielded by dividing the raw image by a background image, which is defined as the average of five consecutive raw images centered at the image to be normalized. The flat-fielded images were projected to a geographic reference frame with a spatial dimension of 300 × 300 km. Complicated structures were present before and during the ripple event. Major phase fronts and propagation directions of four wave trains are sketched in the first image at 1428 UT. Breakdown of wave B into small-scale structures can be seen between 1434 and 1440 UT in the SE quadrant. The letters Z, N, E, S, and W in the image at 1436 UT indicate the positions where lidar measures temperature and winds in the center of the OH airglow layer.

nearly along the N-S direction. More ripple fronts appeared in the subsequent images. In the last image at 145056 UT, approximately nine ripple fronts are seen. The orientation of the phase fronts changed gradually from nearly N-S near the zenith to NNW-SSE away from the zenith. Note that the same structure was observed in Figure 2.

3.2. Lidar Observations

3.2.1. Overview of the Night

[17] Contour plots of the temperature (T), sodium (Na) mixing ratio, zonal wind (u) and meridional wind (v) are displayed in Figure 5. The most prominent feature in the temperature is the downward progression of an inversion layer between ~0800 and 1300 UT. The peak of the inversion layer descended from ~96 km at 0800 UT to ~91 km at 1300 UT, i.e., at a speed of 1 km/hr consistent with the phase speed of upward propagating diurnal tides. The downward phase progression is also seen in the Na mixing ratio during the same period and in the meridional wind between ~0800 and 1100 UT. This structure was less clear in the zonal wind. The most striking feature in the zonal wind is the presence of high wind shear in the height range of ~87–90 km before 1300 UT.

[18] The Na mixing ratio is shown in Figure 5b. We choose to present the Na mixing ratio instead of Na density because the former is a better tracer of wave motion [*Clemesha et al.*, 1982]. The method of *Williams et al.* [2002] is followed to calculate the Na mixing ratio from the Na density and the temperature. A sporadic Na layer, which is characterized by a rapid increase in Na concentration over

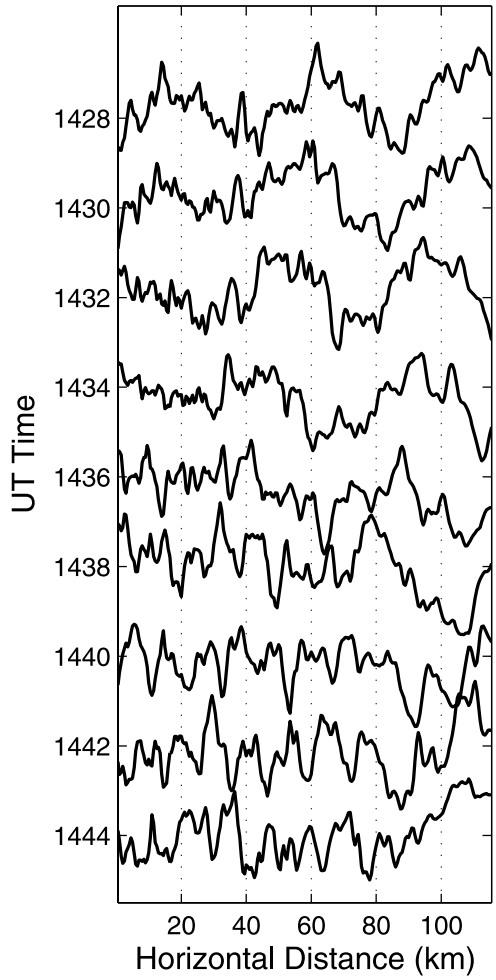

Figure 3. Time evolution of airglow intensities perpendicular to the phase fronts of wave B from 1428 to 1444 UT. The horizontal axis is along the blue lines shown in the image at 1430 UT in Figure 2. The distance increases from left to right. Airglow intensities were averaged over the red line which is along the wave B wave fronts. Very different structures are seen before 1434 UT and after 1440 UT.

a narrow height range [*Qian et al.*, 1998], existed between ~0800 and 1300 UT in the 90–95 km height range. This sporadic Na layer correlated well with the temperature inversion layer. Overturning structures, with high Na mixing ratio over low Na mixing ratio or with nearly vertical contour lines, were found above the sporadic Na layer between ~0900 and 1200 UT. Because Na mixing ratio is a quasi-tracer of the wave motion, overturning in Na mixing ratio indicates similar overturning in potential temperature and suggests wave breaking [e.g., *Williams et al.*, 2002]. To further investigate instabilities associated with the overturning structures, we plot in Figure 6 the Richardson number (Ri), the square of the Brunt-Vaisala frequency (N^2), the magnitude of the zonal wind shear (|dU/dz|) and the magnitude of the meridional wind shear (|dV/dz|). N^2 is defined as

$$N^2 = \frac{g}{T}\left(\frac{dT}{dz} + \frac{g}{c_p}\right), \tag{1}$$

and Ri is defined as

$$Ri = \frac{N^2}{S^2}, \tag{2}$$

where g is the acceleration of gravity, Cp is the specific heat at constant pressure, and $S = \sqrt{\left(\frac{du}{dz}\right)^2 + \left(\frac{dv}{dz}\right)^2}$ is the vertical shear in the horizontal winds. Traditionally, $N^2 < 0$ and $0 < Ri < 0.25$ are treated as critical limits for convective and dynamical instability, respectively.

[19] Note that $0 < Ri < 0.25$ is the necessary but not sufficient condition for dynamical instability, and the condition is derived for plane stratified shear flow [*Miles*, 1961] that may not apply to gravity wave instabilities. Theoretical and modeling studies have suggested that the gravity wave instability process is far more complex than the traditional view. Convective and dynamical instability may occur outside of the assumed critical limit [*Chimonas*, 1986; *Lombard and Riley*, 1996; *Sonmor and Klaassen*, 1997] (for a complete discussion of gravity wave instability dynamics, see the review by *Fritts and Alexander* [2003] and the references therein). The traditional view of instabilities, however, seems to agree with many of the observational studies in the MLT [*Hecht et al.*, 1997, 2001; *Williams et al.*, 2002] and in fact was adopted by *Fritts and Alexander* [2003] as a staring point of their discussion of instability evolution. Therefore we will use the traditional approach to interpret the observations.

[20] Figure 6b shows a thin layer of enhanced N^2 with a width of ~2 km that descended from ~95 km at 0800 UT to ~90 km at 1300 UT. This enhanced N^2 layer was a result of the large positive vertical temperature gradient of the mesopause temperature inversion layer (Figure 5a). The temperature profiles exhibited a double-minimum structure associated with the inversion layer. As a result, the atmospheric static stability was reduced on the top of and just below the inversion layer. Scattered unstable areas ($N^2 < 0$) were found in the two reduced stability layers, primarily in the upper layer (Figure 6b). Note that the overturning in the Na mixing ratio or the nearly vertical contour line of the Na mixing ratio (Figure 5b) were observed in the region of reduced stability above the inversion layer. A high zonal shear layer with magnitudes > 40 m/s/km was located in the height range of ~87–89 km before 1000 UT (Figure 6c). Corresponding to the high zonal wind shear layer, dynamically unstable areas were found at about the same region during the same period (Figure 6a). It is likely that the negative N^2 atop and below the inversion layer, and the high zonal wind shear on the bottom side of the overturning were caused by a large amplitude breaking wave.

[21] The peak of the OH airglow layer is almost always located in the height range of 85–90 km, and Figure 6a shows that the atmosphere was dynamically unstable in that altitude range between ~0800 and 1000 UT, and after 1445 UT. The appearance of the ripples (Figures 1 and 2) just as the dynamical instability formed strongly suggests that the ripple structures are a manifestation of the instability. We will concentrate on the ripple structures around 1445 UT, because the sky was clear during this event, and we will investigate whether the data as a whole are consistent with this hypothesis.

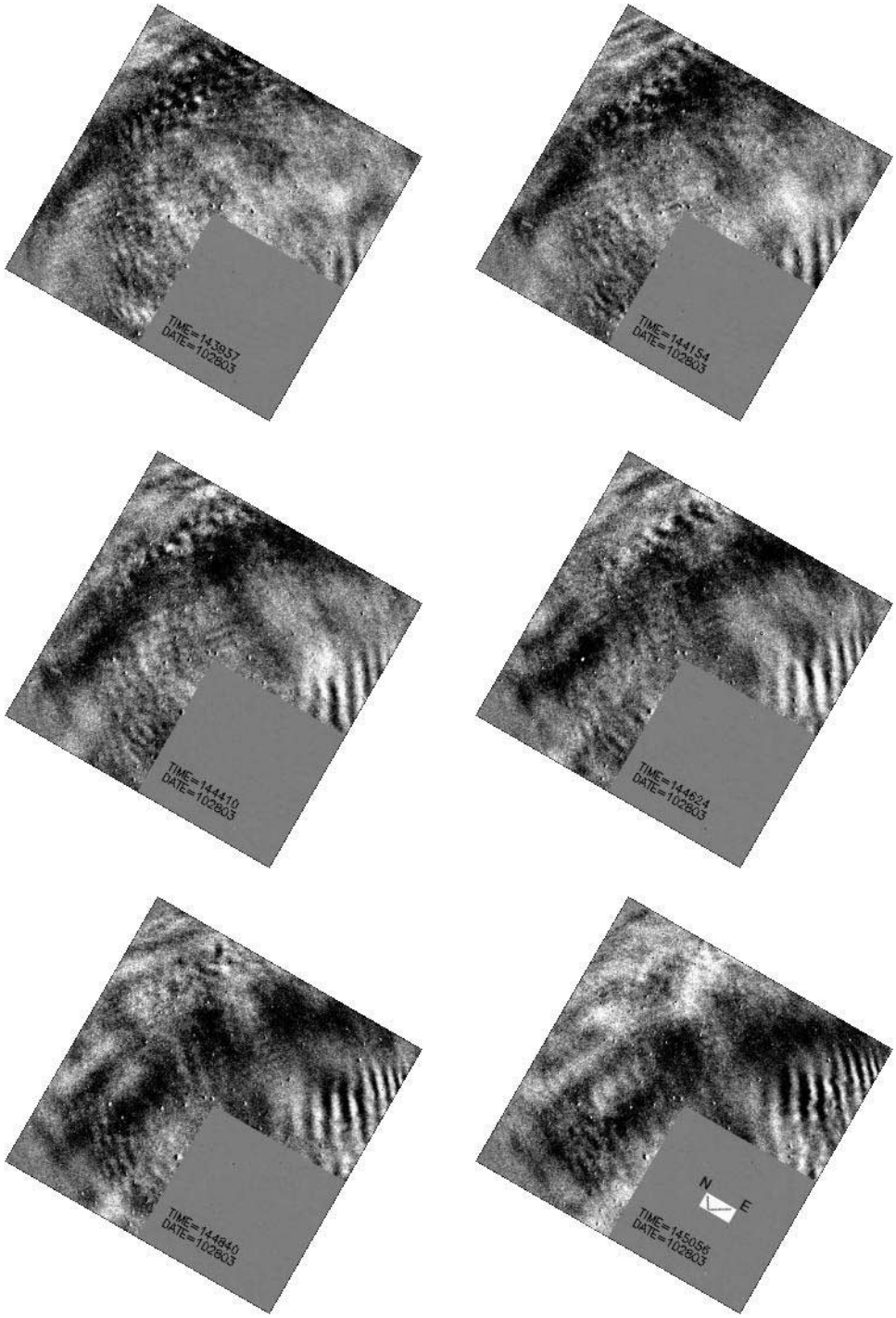

Figure 4. A sequence of time difference images taken by the Aerospace near-infrared camera between ~1440 and 1450 UT. The time difference image is the difference between two subsequent raw images which were taken every 1 min. The time and date are shown in the SE quadrant. The images have been flipped and rotated such that they have the same orientation as that in Figure 2 with north at the top and east to the right. Each image has a size of 256 × 256 pixels. The central 128 pixels correspond to ~61 km.

3.2.2. Kelvin-Helmholtz Billows

[22] In order to investigate whether the ripple event observed between 1440 and 1500 UT was due to dynamical instabilities, profiles of N^2 and Ri in the 85–90 km height range between 1415 and 1500 UT are plotted in Figures 7a and 7b. N^2 profiles show that the background atmosphere was convectively stable during the period when the ripples were observed, while Ri profiles reveal the existence of a dynamically unstable layer around 88 km at 1445 and 1500 UT. It should be noted that N^2 was calculated from 15 min and 0.5 km temporally and vertically averaged temperature profiles. Hence our calculation of N^2 may not

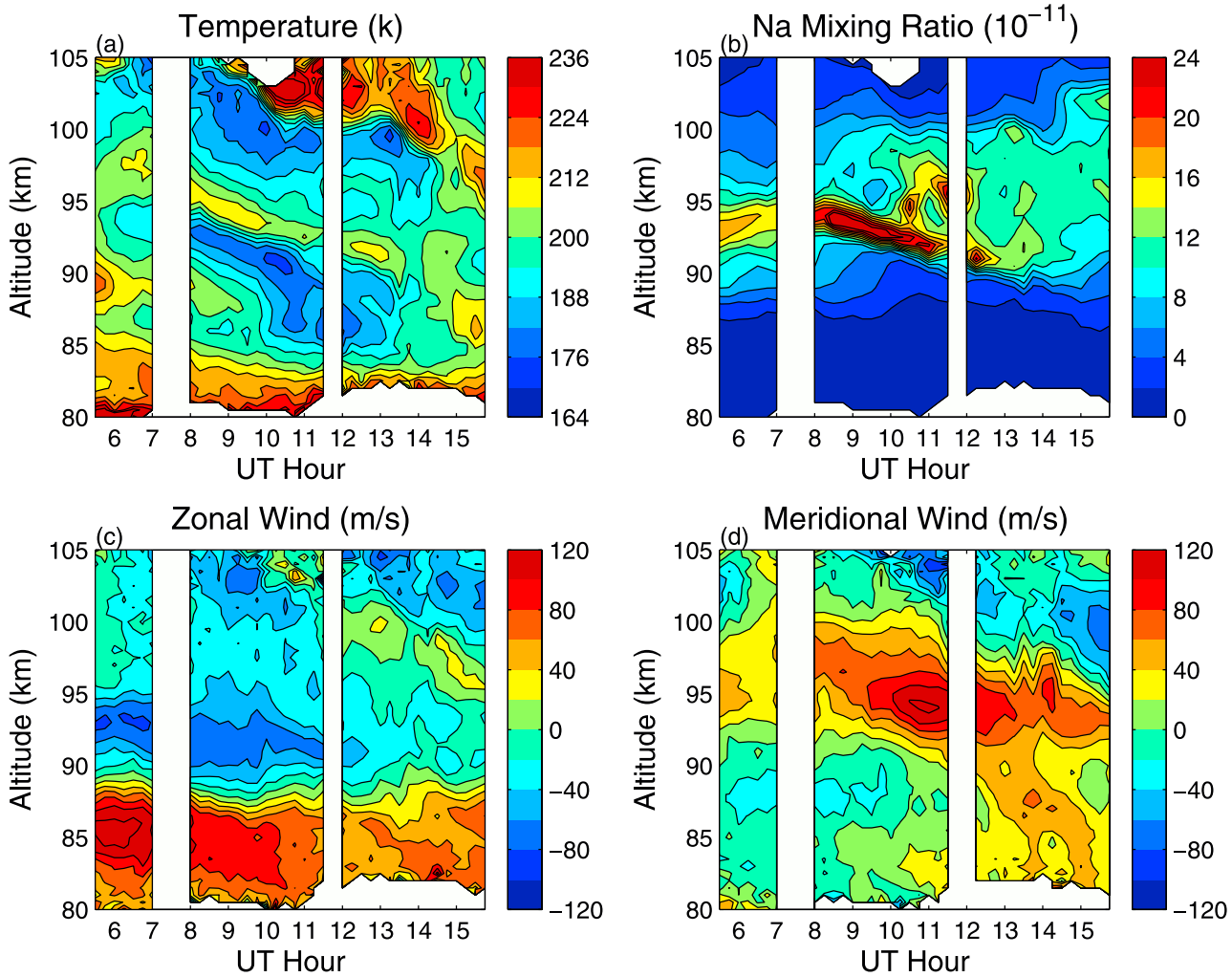

Figure 5. Time-height contour plots of (a) the temperature, (b) the sodium (Na) mixing ratio, (c) the zonal wind, and (d) the meridional wind on the night of 28 October 2003. The data were smoothed to have a vertical resolution of 0.5 km and a temporal resolution of 15 min.

be able to capture unstable temperature structures which existed for only a short period of time or over a very restricted vertical region. In order to confirm that convective instability did not occur, we calculated N^2 using temperature profiles without temporal smoothing between 1430 and 1500 UT (figure not shown). It is found that N^2 was positive above 86 km in all the profiles for this time period. Although a few points are found to have negative N^2 below 86 km, the values were within measurement uncertainty of zero. More importantly, N^2 was well above zero around 88 km where Ri smaller than 0.25 occurred. Small vertical-scale convective instabilities can also be eliminated because the ripple horizontal wavelengths are much larger than can be accounted for by such small-scale vertical convective instabilities [*Fritts et al.*, 1997]. As a result, we conclude that the ripples were not caused by convective instabilities.

[23] Figure 7a shows that Ri > 0.7 in the 88–89.5 km height range at 1415 UT, which is above the assumed dynamical instability limit of Ri = 0.25. At 1430 UT, Ri values of all the 4 points between 88 and 89.5 km decreased, and were close to the nominal value of 0.25 at 88 and 89.5 km. Comparing the time evolutions of the Ri profiles with those of N^2 and horizontal wind shears (Figures 7b, 7c, and 7d) reveals that the systematic decrease of shear stability in this layer was primarily due to an increase of the zonal wind shear in the same region. The enhancement of the zonal wind shear continued and the strong wind shear progressed downward by about 1 km at 1445 UT. The amplitude of the zonal wind shear was close to or greater than 40 m/s/km between 88 and 89 km. These strong wind shears drove Ri to less than or very close to 0.25 in this region (Ri = 0.27, 0.23, and 0.28 at 88, 88.5 and 89 km, respectively). Note that the breakdown of wave B into ripples occurred between 1430 and 1445 UT. At 1500 UT, the strong wind shear and the Ri < 0.25 layer continued to propagate downward by ~1 km. While the traditional criterion of 0 < Ri < 0.25 for dynamical instability is not likely to be correct in all circumstances, our observations of the coincidence of ripples, which are almost certainly a manifestation of instability regions [*Hecht*, 2004], and Ri < 0.25 strongly suggest that a dynamical instability developed and generated the ripples. The resolution of the data is not high enough to distinguish a Ri of marginally stable (e.g., 0.27) to a Ri of marginally unstable

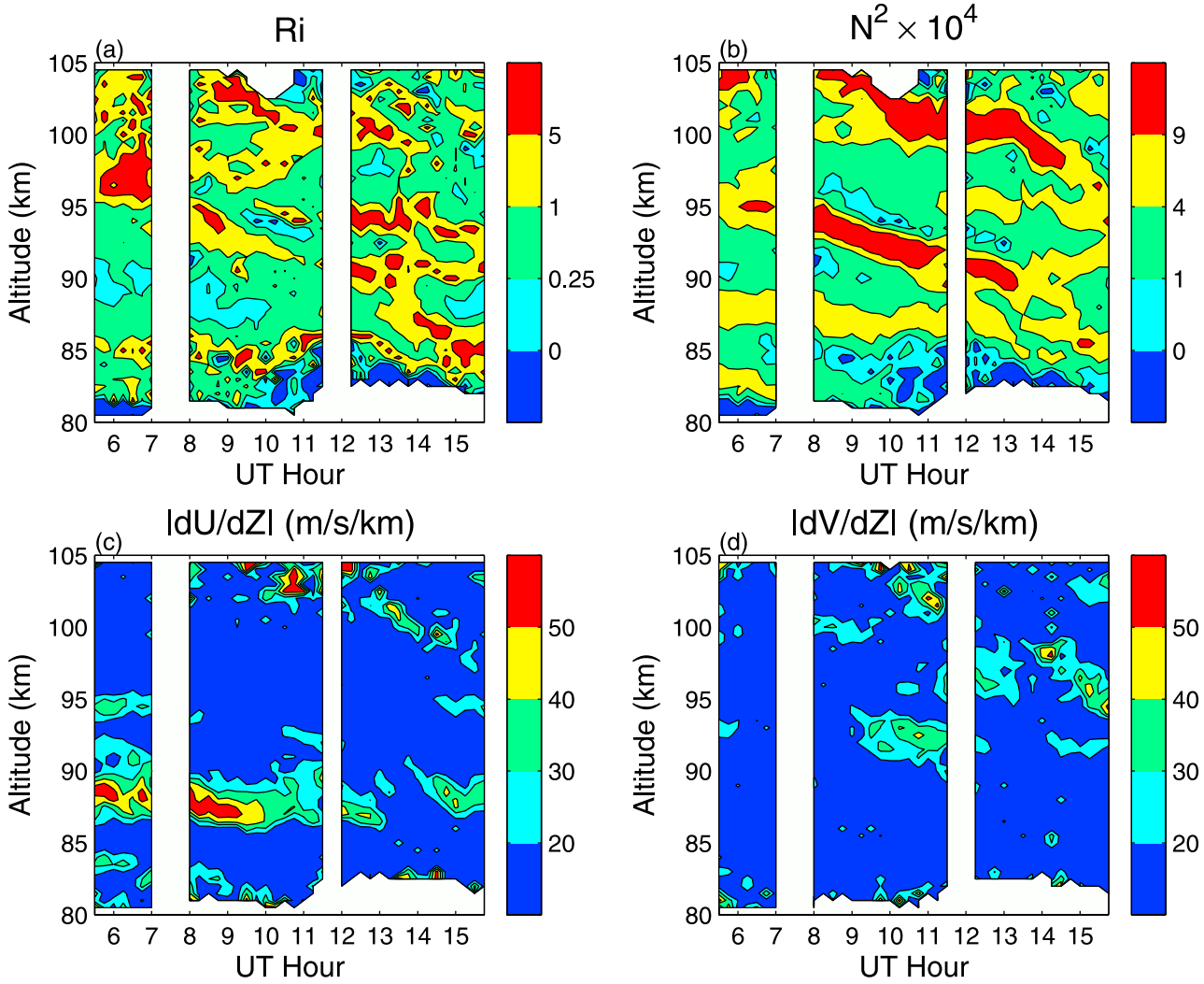

Figure 6. Time-height contour plots of (a) the Richardson number (Ri), (b) the Brunt-Vaisala frequency squared (N^2), (c) the magnitude of the zonal wind shear (|dU/dz|), and (d) the magnitude of the meridional wind shear (|dV/dz|). All fields have a vertical and a temporal resolution of 0.5 km and 15 min, respectively.

(e.g., 0.23), hence we will assume the width of the unstable layer was ~1.5 km. Another concern is that the growth rate for a marginally unstable flow maybe too slow to account for the observed evolution of instability structures. Given that the data were vertically and temporally smoothed, it is likely that the data did not capture the minimum Ri, which is likely to be lower than the observed value.

[24] If the ripples were caused by dynamical (or Kelvin-Helmholtz) instabilities, then the characteristics of the unstable structures, including their alignment with respect to the shear vector, their horizontal separation, and their direction of propagation, should be consistent with those of KH billows.

[25] Theoretical studies have shown that the phase fronts of KH billows typically form perpendicular to the wind shear vector in the unstable layer [*Gossard and Hooke*, 1975]. In the special case when an incident gravity wave is in the direction of the background wind shear, the breaking of the gravity wave can generate KH instability structures parallel to the phase fronts of the parent wave. This is because the mean wind shear favors the amplification and convergence for gravity waves propagating in the same direction. Figure 8 shows the maximum horizontal wind shear vectors between 85 and 90 km at 1430, 1445 and 1500 UT. Note that the wind shears were almost in the same direction of wave B. At 1445 and 1500 UT, after the appearance of the ripples, the maximum horizontal wind shears were located in the unstable layer with a magnitude of ~45 m/s/km. The wind shear vectors were aligned nearly perpendicular to the fronts of the ripples which were oriented NNW-SSE (Figure 2). The alignment of the wind shear vector in the unstable layer is consistent with the explanation that the ripples were KH billows.

[26] The horizontal spacing (d) of KH billows is related to the depth of the shear layer (h) given approximately by d = 8h [*Lloyd et al.*, 1973; *Larsen*, 2000]. The unstable shear layer had a depth of 1–1.5 km (Figure 7a), suggesting that the KH billows should have a horizontal spacing of ~8–12 km. Figure 3 shows that the ripple fronts were

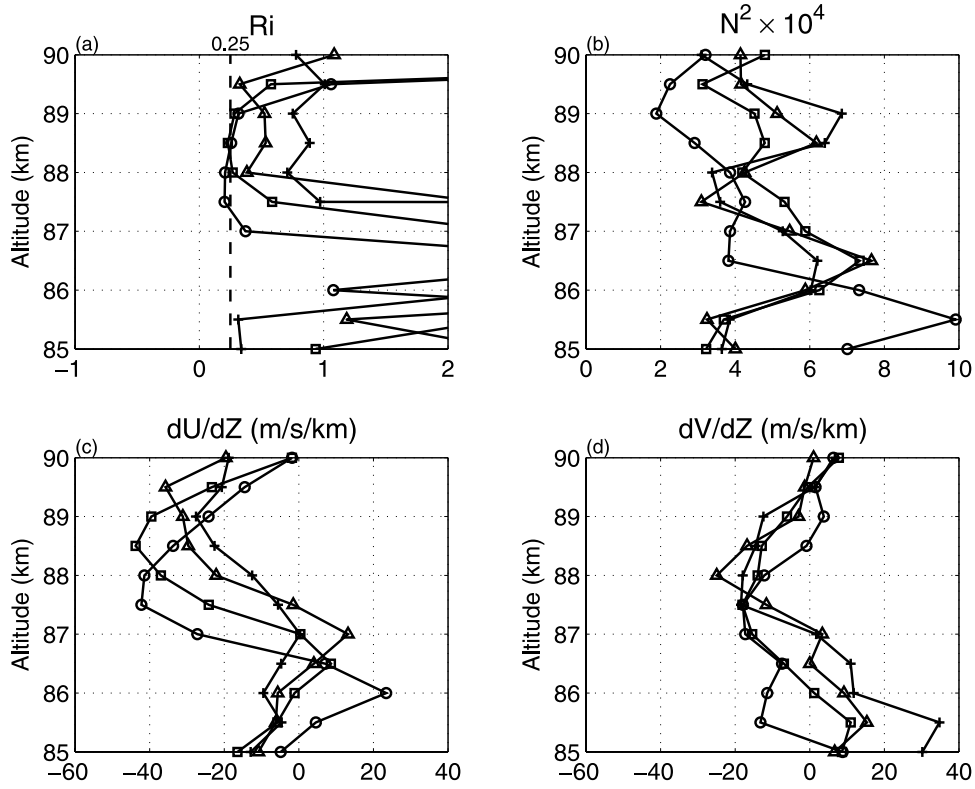

Figure 7. Profiles of (a) Ri, (b) N^2, (c) dU/dz, and (d) dV/dz between 85 and 90 km at 1415 (pluses), 1430 (triangles), 1445 (squares), and 1500 (circles) UT. The dynamical instability limit (Ri = 0.25) is shown by the dashed line in Figure 7a. The atmosphere was dynamically unstable around 88 km during the period when the ripples were observed.

separated by ~12 km, consistent with the theoretical prediction. Structures generated by in situ instabilities tend to move with the mean background wind [*Larsen*, 2000]. The hodograph of horizontal winds at 1445 UT is presented in Figure 9. Below 87 km the horizontal winds were toward NE and the wind speed was close to 80 m/s. Above 87 km the zonal wind decreased dramatically from ~60 m/s to ~−30 m/s at 90 km. The meridional wind speed also decreased, but the change was not as significant. Also plotted in Figure 9 is the estimated motion of the ripple region between 1440 and 1450 UT (thin arrow). There are uncertainties in the estimated ripple movement, because the apparent ripple motion was likely accompanied with growing and decay of the ripples. The ripples moved toward the NE at a speed of ~58 m/s. The direction and speed of the ripple motion agree well with the background wind velocity at 88 km. We have shown that the unstable layer and the strong wind shear were located around 88 km (Figure 7). The agreement of the ripple movement and the mean wind in the unstable layer supports that the instabilities were advected by the background flow. In summary, our data show that the ripples are indeed a manifestation of a dynamical instability as calculated by the traditional approach.

4. Discussion

[27] A possible scenario that might explain the observations is as following: Wave B propagated into a region of marginal dynamical stability, drove the profile to Ri < 0.25, and broke, generating the ripples. The observations strongly support this scenario. Figure 7a shows that at 1430 UT the atmosphere was marginally stable with

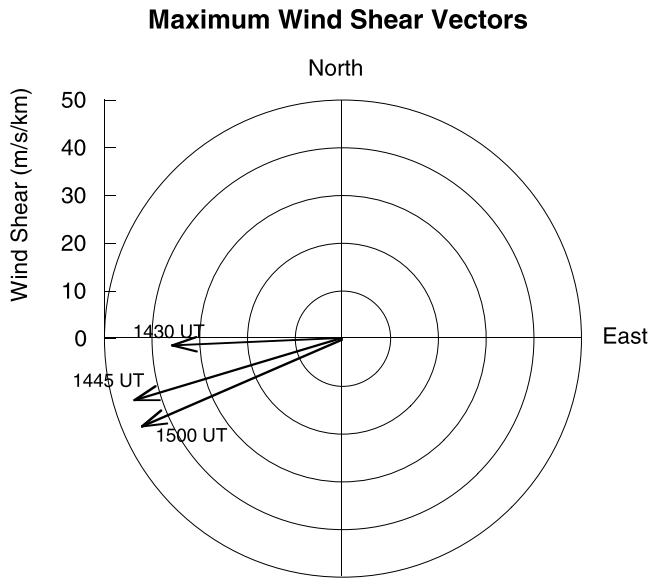

Figure 8. A polar plot of the maximum wind shear vectors in the 85–90 km height range at 1430, 1445, and 1500 UT, which were located at 89.5, 88.5, and 87.5 km, respectively.

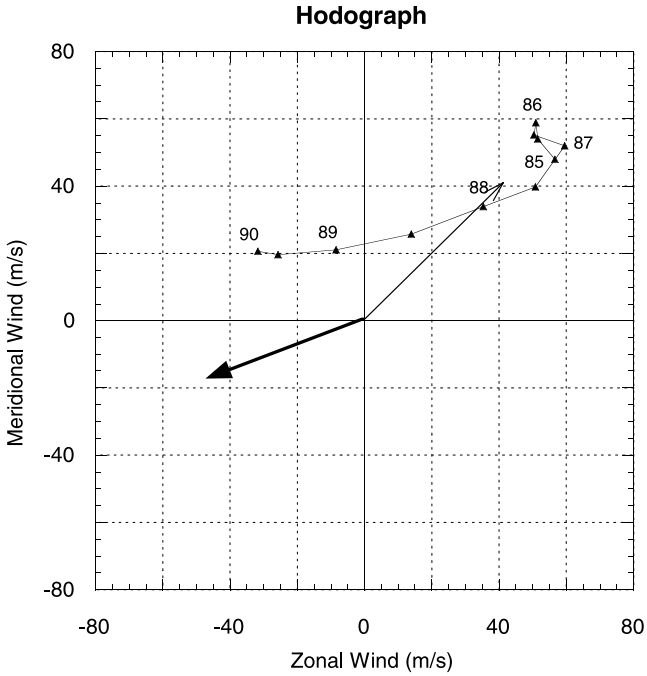

Figure 9. Hodograph in the 85–90 km height range at 1445 UT (triangles). The thick arrow indicates the phase velocity of wave B. The thin arrow is the estimated ripple movement between 1442 and 1450 UT.

Ri < 0.5 between 88 and 89.5 km before the breakdown of wave B. The environmental wind shears at 1430 UT were aligned nearly parallel with the propagation direction of wave B (Figure 8). It is very likely that the superposition of wind shears associated with the background wind and wave B could result in a total wind shear large enough to cause dynamical instabilities sometime between 1430 and 1445 UT, leading to the breakdown of wave B and the generation of KH billows. It is also likely that gravity wave/mean flow interactions contributed to the strong wind shear.

[28] Figure 10 shows the phase velocity of wave B, the maximum wind shear at 1445 UT in the unstable region, and the mean wind acceleration vector in the unstable layer between 1430 and 1445 UT. The most striking feature in Figure 10 is that the wave propagation, the mean flow acceleration, and the wind shear were in the same direction. This unique feature suggests that local mean flow accelerations due to wave-mean flow interactions might significantly contribute to the strong wind shear and instability. It should be emphasized that gravity wave/mean flow interactions precede instability. Before a gravity wave achieves an amplitude large enough to cause instability and break, forcing of the mean flow has already occurred, by means of, for example, the transient growth in wave amplitude.

[29] The downward propagation of the strong wind shear provides additional evidence that wave B was indeed the cause of the instabilities. The maximum wind shears in the 85–90 km height range were found at 89.5, 88.5 and 87.5 km at 1430, 1445 and 1500 UT, respectively (Figure 8). This downward propagation is clearly demonstrated in Figure 7c. The descent of the wind shear, which was almost parallel to the propagation direction of wave B, is consistent with wave B being upward propagating.

[30] *Hecht et al.* [2001] analyzed a ripple event and attributed the ripples to a dynamical instability. They found that the instability was due to a combination of the background shear and a gravity wave induced wind shear. In their case, the large shear induced by the gravity wave was a result of decrease in vertical wavelength when the gravity wave approached a critical layer. Figure 9 shows that wave B is well away from its critical layer. It can be estimated from Figure 9 that the intrinsic phase speed of wave B was in the range of 30–110 m/s between 85 and 90 km at 1445 UT. The intrinsic phase speed of wave B at 1415 and 1430 UT was larger than 40 m/s in the OH airglow layer (figure not shown).

[31] Figure 10 shows that the local mean flow was accelerated toward the propagation direction of wave B by 17 m/s between 1430 and 1445 UT. The acceleration was larger at the top of the unstable layer at 89 and 89.5 km with an increase of westward zonal wind of >20 m/s in 15 min. Part of the local mean flow acceleration should be attributed to wave breaking. The body force due to wave B breaking can be estimated if we assume all the momentum flux of wave B is deposited into the mean flow. *Swenson and Liu* [1998] developed a method to calculate the

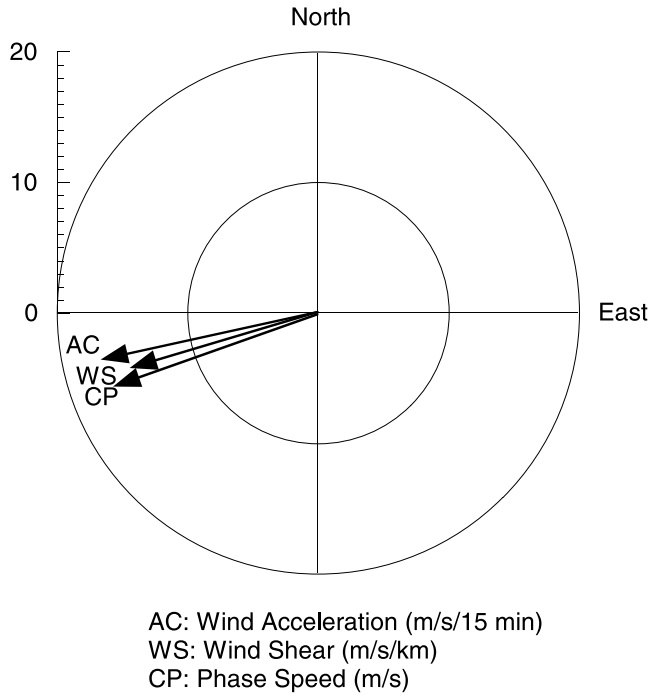

Figure 10. A polar plot of the observed phase velocity of wave B (CP), the maximum wind shear at 1445 UT (WS), and the wind acceleration in the unstable layer at 1445 UT (AC). AC was calculated as the difference of the mean wind velocity in the 88–89 km range between 1430 and 1445 UT. The magnitudes of WS and CP have been reduced by a factor of 3.

momentum flux of a monochromatic gravity wave using wave induced OH airglow intensity perturbations as

$$F_m = \frac{1}{2}\frac{\lambda_z}{\lambda_h}\frac{g^2}{N^2}\frac{\left(I'/I_0\right)^2}{\eta^2}, \quad (3)$$

where $\frac{I'}{I_0}$ is the amplitude (mean to peak) of relative airglow intensity perturbations, and $\eta = \frac{I'/I_0}{T'/T_0}$ is the cancellation factor defined as the ratio of relative airglow intensity amplitude to the relative temperature amplitude. The relative airglow intensity amplitude $\frac{I'}{I_0}$ of wave B is ~5% derived from raw images. The cancellation factor of wave B is ~3.5 with a vertical wavelength of 35 km [*Swenson and Gardner*, 1998]. Given g = 9.5 m^2s^{-2}, N = 0.02 s^{-1}, λ_h = 44 km and λ_z = 35 km, the momentum flux of wave B is estimated to be ~18 m^2s^{-2}.Assuming that all the momentum flux is deposited to the mean flow and that the momentum flux divergence is confined within the unstable layer, the resulting mean flow acceleration is 16 m/s in 15 min (estimated using *Fritts et al.* [2002, equation (1)] by assuming H = 1 km). The estimated body force is comparable with the observed ~17 m/s local mean flow acceleration between 1430 and 1445 UT. The estimated mean flow acceleration could be smaller, because it is likely only part of the wave momentum flux transferred to mean flow. Nevertheless, this estimate suggests that wave-mean flow interactions can have significant impacts on the local mean flow. It should be noted that only ~10% of the wind accelerations for the night between 85 and 100 km were larger than 20 m/s/15 min, and only ~3.6% of the zonal wind accelerations had a magnitude larger than 20 m/s/15 min. Although we cannot prove every rapid wind change was associated with a gravity wave or with wave breaking, we found that the overturning structures in the Na mixing ratio were accompanied by rapid wind accelerations, which is consistent with the above discussion.

5. Summary

[32] Simultaneous measurements from airglow imager and Na wind/temperature lidar colocated at Maui, HI were used to investigate the breakdown of a gravity wave into small-scale ripples in OH airglow on the night of 28 October 2003. The ripples had a horizontal separation of ~12 km and lasted ~20 min. We suggest that the generation of ripples were caused by dynamical instabilities based on the following observations:

[33] 1. The environment was convectively stable in the OH airglow layer during the period when the ripples were observed, while there existed a dynamically unstable layer around 88 km with a ~1–1.5 km depth during the same period.

[34] 2. The wave fronts of the ripples were aligned nearly perpendicular to the wind shear vector in the unstable layer.

[35] 3. The horizontal separation of the ripples was about 8 times of the depth of the unstable layer.

[36] 4. The ripples appeared to be advected by the background flow.

[37] Before breaking, wave B propagated in the same direction of the mean wind shear. Observations suggest that a dynamical instability occurred in a region of superposition of the mean wind shear and the wave shear. Mean flow accelerations due to momentum transfer from wave B likely contributed to the observed strong wind shear and the generation of the dynamical instability. Interestingly, our observations are similar to complex 3-D numerical simulations of gravity wave instability process [e.g., *Fritts et al.*, 1994, 1998; *Andreassen et al.*, 1994, 1998]. These numerical studies found that, when a gravity wave propagates in the same direction of the mean wind shear, the superposed wind shear favors the generation of KH shear instability. Clearly, a combination of numerical and observational studies is needed for a better understanding of wave instability dynamics.

[38] **Acknowledgments.** FL, AZL, and GRS acknowledge support from NSF grants ATM-00-03198 in support of the Maui MALT lidar, ATM-00-03180 in support of Maui MALT airglow imager, and NASA NAG 5-13593 in support of SOR observations at Albuquerque, NM, and now Socorro, NM. JHH was supported by NSF grant ATM-0122772 and under The Aerospace Corporation's Mission Oriented Investigation and Experimentation program, funded by the U.S. Air Force Space and Missile Systems Center under contract FA8802-04-C-0001. WR is supported by NSF grant ATM-00-02724. Special appreciations extended to the USAF and Boeing personnel at Maui for support of lidar telescope operations, to University of Illinois Research Scientist Xinzhao Chu, and to graduate students Chirantan Mukhopodyay and Jeff Bruggemann for lidar operations and maintenance. The authors want to thank two anonymous reviewers for their valuable suggestions.

References

Andreassen, O., C. E. Wasberg, D. C. Fritts, and J. R. Isler (1994), Gravity wave breaking in two and three dimensions: 1. Model description and comparison of two-dimensional evolutions, *J. Geophys. Res.*, *99*, 8095–8108.

Andreassen, O., P. O. Hvidsten, D. C. Fritts, and S. Arendt (1998), Vorticity dynamics in a breaking internal gravity wave. part 1. Initial instability evolution, *J. Fluid Mech.*, *367*, 27–46.

Chimonas, G. (1986), The combined Rayleigh, Kelvin-Helmholtz problem, *Phys. Fluids*, *29*(7), 2061–2066.

Clemesha, B. R., D. M. Simonich, P. P. Batista, and W. J. H. V.Kirchhoff (1982), The diurnal variation of atmosphere sodium, *J. Geophys. Res.*, *87*, 181–186.

Fritts, D. C., and M. J. Alexander (2003), Gravity wave dynamics and effects in the middle atmosphere, *Rev. Geophys.*, *41*(1), 1003, doi:10.1029/2001RG000106.

Fritts, D. C., J. R. Isler, and O. Andreassen (1994), Gravity wave breaking in two and three dimensions: 2. Three dimensional evolution of instability structure, *J. Geophys. Res.*, *99*, 8109–8123.

Fritts, D. C., J. R. Isler, J. H. Hecht, R. L. Walterscheid, and O. Andreassen (1997), Wave breaking signatures in sodium densities and OH nightglow: 2. Simulation of wave and instability structures, *J. Geophys. Res.*, *102*, 6669–6684.

Fritts, D. C., S. Ardndt, and O. Andreassen (1998), Vorticity dynamics in a breaking internal gravity wave. part 2. Vortex interactions and transition to turbulence, *J. Fluid Mech.*, *367*, 47–65.

Fritts, D. C., S. L. Vadas, and Y. Yamada (2002), An estimate of strong local body forcing and gravity wave radiation based on OH airglow and meteor radar observations, *Geophys. Res. Lett.*, *29*(10), 1429, doi:10.1029/2001GL013753.

Gardner, C. S., and G. C. Papen (1995), Mesospheric Na wind/temperature lidar, *Rev. Laser Eng.*, *23*, 131–134.

Gossard, E. E., and W. H. Hooke (1975), *Waves in the Atmosphere*, 456 pp., Elsevier Sci., New York.

Hecht, J. H. (2004), Instability layers and airglow imaging, *Rev. Geophys.*, *42*, RG1001, doi:10.1029/2003RG000131.

Hecht, J. H., R. L. Walterscheid, D. C. Fritts, J. R. Isler, D. C. Senft, C. S. Gardner, and S. J. Franke (1997), Wave breaking signatures in OH airglow and sodium densities and temperature: 1. Airglow imaging, Na lidar, and MF radar observations, *J. Geophys. Res.*, *102*, 6655–6668.

Hecht, J. H., C. Friche-Begemann, R. L. Walterscheid, and J. Hoffner (2000), Observations of the breakdown of an atmospheric gravity wave near the cold summer mesopause at 54°N, *Geophys. Res. Lett.*, *27*, 879–882.

Hecht, J. H., R. L. Walterscheid, and R. A. Vincent (2001), Airglow observations of dynamical (wind shear-induced) instabilities over Adelaide, Australia, associated with atmospheric gravity waves, *J. Geophys. Res.*, *106*, 28,189–28,197.

Hecht, J. H., A. Z. Liu, R. L. Walterscheid, and R. J. Rudy (2005), Maui Mesosphere and Lower Thermosphere (Maui MALT) observations of the evolution of Kelvin-Helmholtz billows formed near 86 km altitude, *J. Geophys. Res.*, *110*, D09S10, doi:10.1029/2003JD003908.

Larsen, M. F. (2000), A shear instability seeding mechanism for quasiperiodic radar echoes, *J. Geophys. Res.*, *105*, 24,931–24,940.

Li, F., A. Z. Liu, and G. R. Swenson (2005), Characteristics of instabilities in the mesopause region over Maui, Hawaii, *J. Geophys. Res.*, *110*, D09S12, doi:10.1029/2004JD005097.

Lloyd, K. H., C. H. Low, and R. A. Vincent (1973), Turbulence, billows, and gravity waves in a high shear region of the upper atmosphere, *Planet. Space Sci.*, *21*, 653–661.

Lombard, P. N., and J. J. Riley (1996), Instability and breakdown of internal gravity waves. 1. Linear stability analysis, *Phys. Fluids*, *8*, 3271–3287.

Miles, J. W. (1961), On the stability of heterogeneous shear flows, *J. Fluid Mech.*, *10*, 496–508.

Nakamura, T., A. Higashikawa, T. Tsuda, and Y. Matsushita (1999), Seasonal variations of gravity wave structures in OH airglow with a CCD imager at Shigaraki, *Earth Planets Space*, *51*, 897–906.

Peterson, A. W. (1979), Airglow events visible to the naked eyes, *Appl. Opt.*, *22*, 3390–3393.

Qian, J., Y. Gu, and C. S. Gardner (1998), Characteristics of the sporadic Na layers observed during the Airborne Lidar and Observations of Hawaiian Airglow/Airborne Noctilucent Cloud (ALOHA/ANLC-93) campaigns, *J. Geophys. Res.*, *103*, 6333–6347.

Rezaul, H., and G. R. Swenson (1999), Extraction of motion parameters of gravity-wave structures from all-sky OH image sequences, *Appl. Opt.*, *38*, 4433–4442.

Sonmor, L. J., and G. P. Klaassen (1997), Toward a unified theory of gravity wave breaking, *J. Atmos. Sci.*, *54*, 2655–2680.

Swenson, G. R., and P. J. Espy (1995), Observations of two-dimensional airglow structure and Na density from the ALOHA, October 9, 1993, "storm flight," *Geophys. Res. Lett.*, *22*, 2845–2848.

Swenson, G. R., and C. S. Gardner (1998), Analytical models for the response of mesospheric Na and OH layers to atmospheric gravity waves, *J. Geophys. Res.*, *103*, 6271–6294.

Swenson, G. R., and A. Z. Liu (1998), A model for calculating acoustic gravity wave energy and momentum flux in the mesosphere from OH airglow, *Geophys. Res. Lett.*, *25*, 477–480.

Swenson, G. R., M. J. Alexander, and R. Hague (2000), Dispersion imposed limits on atmospheric gravity waves in the mesosphere: Observations from OH airglow, *Geophys. Res. Lett.*, *27*, 875–878.

Taylor, M. J., and M. A. Hapgood (1990), On the origin of ripple-type wave structure in the OH nightglow emission, *Planet. Space Sci.*, *38*, 1421–1430.

Taylor, M. J., and M. J. Hill (1991), Near infrared imaging of hydroxyl wave structure over an ocean site at low latitudes, *Geophys. Res. Lett.*, *18*, 1333–1336.

Taylor, M. J., D. C. Fritts, and J. R. Isler (1995), Determination of horizontal and vertical structure of an unusual pattern of short period gravity waves imaged during ALOHA-93, *Geophys. Res. Lett.*, *22*, 2837–2840.

Walterscheid, R. L., J. H. Hecht, R. A. Vincent, I. M. Reid, J. Woithe, and M. P. Hickey (1998), Analysis and interpretation of airglow and radar observations of quasi-monochromatic gravity wave in the upper mesosphere and lower thermosphere over Adelaide (35°S, 138°E), *J. Terr. Sol. Atmos. Phys.*, *61*, 461–478.

Williams, B. P., M. A. White, D. A. Krueger, and C. Y. She (2002), Observation of a large amplitude wave and inversion layer leading to convective instability in the mesopause region over Fort Collins, CO (41°N, 105°W), *Geophys. Res. Lett.*, *29*(17), 1850, doi:10.1029/2001GL014514.

Yamada, Y., H. Fukunishi, T. Nakamura, and T. Tsuda (2001), Breaking of small-scale gravity wav and transition to turbulence observed in OH airglow, *Geophys. Res. Lett.*, *28*, 2153–2156.

J. H. Hecht, Space Science Application Laboratory, The Aerospace Corporation, Mail Stop M2-259, PO Box 92957, Los Angeles, CA 90009, USA.

F. Li and W. A. Robinson, Department of Atmospheric Sciences, University of Illinois at Urbana-Champaign, 1308 West Main Street, Urbana, IL 61801, USA. (fengli@uiuc.edu)

A. Z. Liu and G. R. Swenson, Department of Electrical and Computer Engineering, University of Illinois at Urbana-Champaign, 1308 West Main Street, Urbana, IL 61801, USA.